Journal of Materials Processing Tech. 353 (2026) 119332

Contents lists available at ScienceDirect

Journal of Materials Processing Tech.

journal homepage: www.elsevier.com/locate/jmatprotec

Research article

Laser scan-path-driven texture selection and sharpening in PBF-LB/M of Inconel 625

Oumayma Elmaalouf [a,b], Patrice Peyre [a], Stefan Dietrich [b], Corinne Dupuy [a], Justin Dirrenberger [a,c,*]

[a] Laboratoire PIMM, Arts et Métiers Institute of Technology, CNRS, CNAM, 151 Boulevard de l'Hôpital, 75013 Paris, France
[b] Institute of Applied Materials (IAM-WK), Karlsruhe Institute of Technology (KIT), 76131 Karlsruhe, Germany
[c] Institut Universitaire de France (IUF), France

ARTICLE INFO

Keywords:
PBF-LB/M
Inconel 625
Crystallographic texture
Scan-path design
Scan-vector length
Texture-controlled mechanical response

ABSTRACT

Crystallographic texture in powder bed fusion by laser beam melting (PBF-LB/M) strongly influences the anisotropic mechanical response of metallic components. However, for Inconel 625 (IN625), it remains insufficiently understood how laser scan-path design governs not only the selection of the dominant texture component, but also the extent to which this component sharpens during solidification. In particular, the respective roles of scan angle, melt-pool geometry, remelting continuity, and scan-vector length (SVL) remain only partially separated in the literature. To address this issue, the present work investigates the influence of laser scan-path design on melt-pool morphology, crystallographic texture, and the resulting mechanical response in PBF-LB/M IN625 through a combined analysis of melt-pool geometry, electron backscatter diffraction, and tensile behaviour. The results show that scan angle primarily controls texture selection along the scanning direction, with dominant ⟨111⟩ and ⟨001⟩ components obtained for $\alpha = 35°$ and $\alpha = 90°$, respectively, whereas melt-pool geometry and remelting continuity govern texture sharpening. Conditions combining higher overlap (up to 69%), flatter melt-pool bottom profiles, and more continuous remelting produced the strongest textures, with texture indices up to $J = 10$, while more curved melt-pool geometries and larger effective non-remelted regions promoted competing grain growth and weaker sharpening. Short SVL introduced a distinct band-filling thermal regime that further modified competitive epitaxial growth independently of nominal energy input, increasing the texture index from $J = 3.4$ at SVL = 0.5 mm to $J = 6.0$ at SVL = 1.0 mm. These scan-induced texture states translated into measurable mechanical differences along the scanning direction: the ⟨111⟩ dominated condition reached a UTS of ~910 MPa with 24.5% elongation, compared with ~769 MPa and 16.0% for the ⟨001⟩ dominated condition. Overall, this work establishes a transferable process–melt-pool–texture–property framework showing that laser scan-path design can be used as a practical lever for crystallographic texture control in PBF-LB/M alloys.

1. Introduction

Additive manufacturing (AM) produces components directly from digital models by successively joining material layer by layer, in contrast to subtractive or formative routes [1]. Within AM, powder bed fusion by laser beam melting (PBF-LB/M), also historically referred to as laser powder bed fusion (LPBF) or selective laser melting (SLM), uses a focused laser to selectively melt metallic powder according to sliced CAD data and can achieve near-full density in metallic components [2,3].

Beyond geometric freedom, PBF-LB/M provides unusual opportunities for microstructure control. Because heat is introduced locally and repeatedly, solidification is highly directional and strongly affected by epitaxial growth, remelting, and steep thermal gradients, which frequently generate pronounced crystallographic textures [3,4]. As a result, scan-path design and processing conditions do not only determine part density and melt-pool dimensions, but also influence the local solidification pathway and the resulting grain structure [5,6].

Recent studies have demonstrated that several processing levers can be used to modify texture formation in PBF-LB/M [7]. Scan-pattern design and interlayer rotation can redirect epitaxial growth and promote distinct preferred orientations [8,9]. Likewise, changes in scan speed or effective energy input can alter melt-pool morphology and thereby modify competitive grain growth and texture selection [10,11]. Even

* Correspondence to: Laboratoire PIMM, 151 Boulevard de l'Hôpital, 75013 Paris, France.
E-mail address: Justin.DIRRENBERGER@ensam.eu (J. Dirrenberger).

https://doi.org/10.1016/j.jmatprotec.2026.119332
Received 30 January 2026; Received in revised form 29 April 2026; Accepted 29 April 2026
Available online 8 May 2026

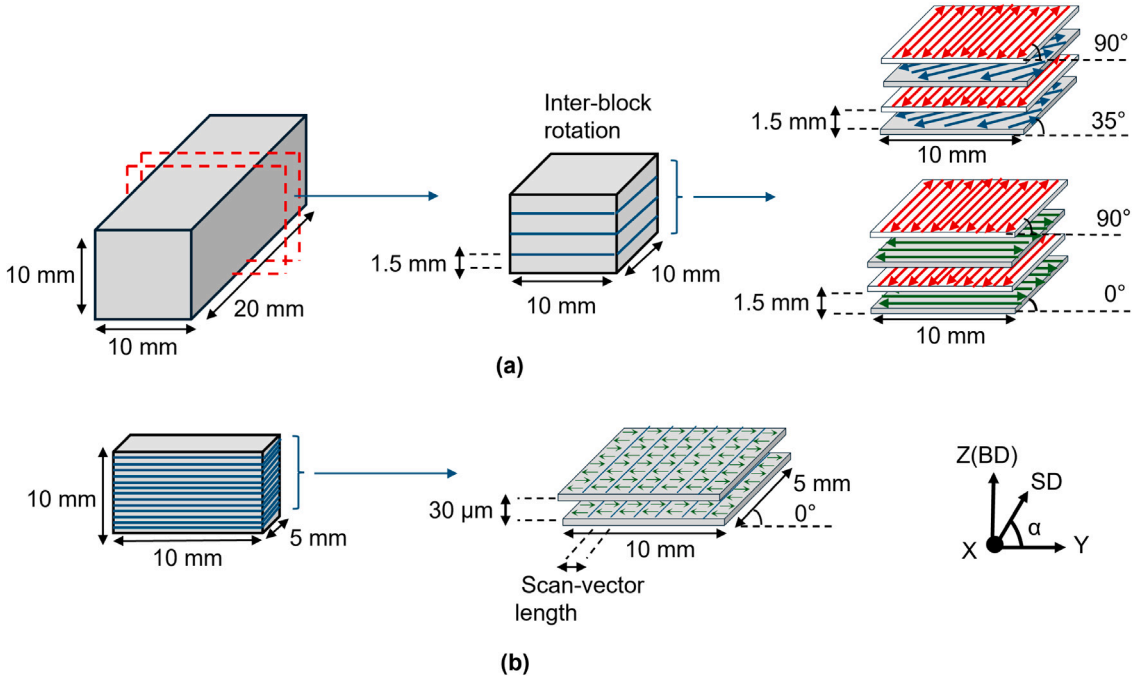

Fig. 1. Build schemes used in the present study. (a) Bulk specimens ($20 \times 10 \times 10$ mm^3) were sectioned into $10 \times 10 \times 10$ mm^3 cubes and fabricated using an inter-block rotation strategy with blocks of 1.5 mm height. Two alternating scan-angle combinations were employed: 90°/35° and 90°/0°. (b) Thin specimens ($5 \times 10 \times 10$ mm^3) were used to vary the scan-vector length while keeping all other process parameters constant, using a 0° scan strategy and a layer thickness of 30 µm. BD denotes the build direction, SD the scan direction, and α the angle between SD and the Y axis.

at comparable nominal volumetric energy density (VED), the relative orientation between scan direction and shielding-gas flow can shift the melt-pool regime and produce markedly different textures, highlighting that nominal energy input alone does not uniquely describe the thermal history experienced by the material [12]. More recently, scan-vector length (SVL) has also emerged as a potentially important control parameter, since shortening the vector modifies local heat accumulation, overlap conditions, and vector-end transients, which in turn affect melt-pool geometry and grain development [13,14].

Taken together, these studies establish that texture engineering in PBF-LB/M can be approached through several process levers, including scan pattern, scan speed, energy input, gas-flow interaction, scan-vector length, and part geometry [14,15]. However, the process–texture link remains fragmented. In particular, it remains insufficiently clarified how scan-path design modifies melt-pool geometry, remelting continuity, and the persistence of the local heat-flow direction, and how these factors separately govern: (i) the selection of the dominant texture component, and (ii) the sharpening or weakening of that component. This distinction is important because many previous studies show that texture can be altered by changing process parameters, but they do not always distinguish whether a given process lever primarily changes the nature of the selected orientation or the extent to which that orientation can develop and persist.

This question is especially relevant for Inconel 625 (IN625), a technologically important Ni-based alloy widely processed by PBF-LB/M for high-temperature and corrosive-service applications. Systematic studies that separate scan-angle effects, nominal processing effects, and scan-vector-length effects within a unified framework remain more limited for IN625.

The objective of the present study is therefore to establish a coherent process–melt-pool–texture framework for PBF-LB/M IN625. First, a dense bidirectional baseline is established and the effects of laser power P, scan speed v, and hatch spacing h on melt-pool morphology and texture development are quantified. Second, the mechanical consequences of the resulting texture states are assessed through orientation-sensitive elastic and plastic indicators, complemented by tensile validation along the scanning direction. Third, scan-vector length is examined as a mechanistic scan-path variable to assess whether shortening the vector is associated with a distinct short-SVL thermal regime, characterized by repeated vector-end transients and local heat accumulation, and whether this regime modifies texture development even when accompanied by processing trade-offs. Beyond the specific IN625 case, the study aims to clarify how scan-path design can be used to control crystallographic texture through its influence on melt-pool geometry, remelting continuity, and local solidification conditions rather than through nominal energy input alone. In the longer term, this framework is intended to support the design of PBF-LB/M components with spatially controlled texture states, combined with mechanical characterization and micromechanical modelling to establish quantitative structure–property relationships.

Table 1
Elemental composition of IN625 (wt%).

Element	Cr	Mo	Nb	Al	Si	Fe	Co	Ni
wt%	21.41	8.98	3.71	0.22	0.11	1.00	0.10	balance

2. Materials and methods

2.1. Materials and sample fabrication method

A gas-atomized IN625 powder (Aubert & Duval) was employed. The nominal composition is listed in Table 1. The particle-size distribution (ASTM B822/ISO 4497) yielded D_{10} = 13.5 µm, D_{50} = 28.8 µm, and D_{90} = 53.7 µm. All builds were produced on an SLM125 equipped with a 400 W Yb:YAG fibre laser. The laser spot diameter at focus was 73 µm, and the nominal layer thickness was 30 µm. The chamber atmosphere consisted of argon with an oxygen content maintained below 100 ppm. To limit thermal gradients and residual stress formation, the build plate was preheated to 150 °C.

Process parameters, laser power (P), scan speed (v), hatch distance (h), and scan strategy were experimentally tuned within a stable

Table 2
First experimental setup: PBF-LB/M process parameters, nominal energy-density condition, porosity (mean ± standard deviation), and scan strategy.

Sample	P (W)	v (mm/s)	h (mm)	Condition	E (J/mm^3)	Porosity (%)	Strategy
S1	200	900	0.09	E1	82.30	0.006 ± 0.003	35°/90° blocks
S2	200	900	0.09		82.30	0.093 ± 0.130	0°/90° blocks
S3	200	900	0.06	E2	123.45	0.036 ± 0.010	35°/90° blocks
S4	200	900	0.06		123.45	0.029 ± 0.023	0°/90° blocks
S5	150	450	0.05	E3	222.22	0.068 ± 0.023	35°/90° blocks
S6	150	450	0.05		222.22	0.065 ± 0.041	0°/90° blocks
TS1	150	450	0.05	E3	222.22	–	35° unidirectional
TS2	150	450	0.05		222.22	–	90° unidirectional

Table 3
Second experimental setup: PBF-LB/M process parameters, scan-vector length (SVL), porosity (mean ± standard deviation), and scan strategy.

Sample	P (W)	v (mm/s)	h (mm)	SVL (mm)	E (J/mm^3)	Porosity (%)	Strategy
S7	200	900	0.12	1.0	61.72	1.295 ± 0.204	0° unidirectional
S8	200	900	0.12	0.5	61.72	1.504 ± 0.114	0° unidirectional

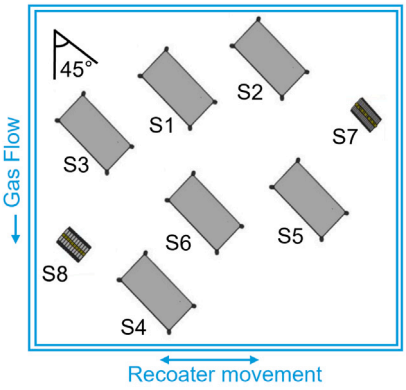

Fig. 2. Top view of the sample arrangement on the build plate. Specimens S1–S6 were rectangular samples positioned at 45° relative to the gas-flow direction. Samples S7 and S8 were fabricated from the same material but with a different geometry and build strategy. The gas-flow direction and recoater movement are indicated for reference.

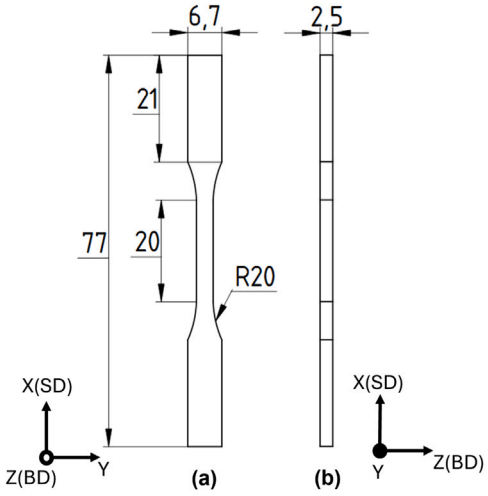

Fig. 3. Geometry and orientation of the flat dog-bone tensile specimens used for macroscopic testing. The tensile axis was aligned with X (scan direction SD). (a) Front view showing the main specimen dimensions. (b) Side view showing the specimen thickness. TS1 corresponds to specimens fabricated with a 35° scan strategy, associated with a ⟨111⟩ dominated texture along SD, whereas TS2 corresponds to specimens fabricated with a 90° scan strategy, associated with a ⟨100⟩ dominated texture along SD.

processing environment to enable crystallographically architectured microstructures. Unless otherwise noted, a bidirectional (zig-zag) raster was used. The laser scan angle α was defined in the plane perpendicular to the build direction (BD), and was varied systematically to probe its influence on grain growth and texture.

Two sets of parallelepiped specimens were fabricated (Fig. 1). The first set (samples S1–S6) had nominal dimensions 20 mm × 10 mm × 10 mm and incorporated scan angles α of 0°, 35° and 90° with no inter-layer rotation. These angles were selected to induce site-specific texture components, following the approach of [7]: ⟨001⟩ for α = 90°, ⟨101⟩ for α = 0°, and ⟨111⟩ for α = 35°. The first build set comprised two alternating-block architectures, 90°/35° and 90°/0°, fabricated without interlayer rotation. EBSD, porosity, and microstructure analyses were performed within the interior of individual blocks, sufficiently far from the block interfaces.

Accordingly, the labels α = 35°, α = 90°, and α = 0° used throughout this work refer to the local scan angle of the analysed block, whereas the interfaces/transition zones between adjacent blocks were not considered. The process parameters were defined using Eq. (1) and are summarized in Table 2.

$$E = \frac{P}{v \cdot h \cdot t} \tag{1}$$

where P represents the laser power (w), v the scan speed (mm/s), h the hatch spacing (mm), and t the layer thickness (mm).

A second geometry, 5 mm × 10 mm × 10 mm (samples S7–S8), was produced to examine the effect of reducing the scan-vector length (SVL) on microstructure and texture development; the corresponding conditions are listed in Table 3. This experimental layout allows (i) direct assessment of scan-angle and process-parameter effects on melt-pool morphology, microstructure, and texture, and (ii) comparison between the two short-SVL conditions (0.5 mm to 1.0 mm) under identical nominal processing parameters. The conventional long-vector condition (~10 mm) from the first set is retained as a qualitative reference for contrast with the short-SVL regime. All specimens were oriented at 45° relative to the shielding-gas flow (Fig. 2), a configuration previously shown to reduce direct scan–gas-flow coupling and to improve melt-pool stability [12].

2.1.1. Tensile specimen geometry and testing

For macroscopic mechanical validation, additional tensile specimens were fabricated separately using homogeneous scan-angle conditions of 35° and 90° (TS1 and TS2 in Table 2). This design ensured that the gauge section corresponded to a single, texture-controlled

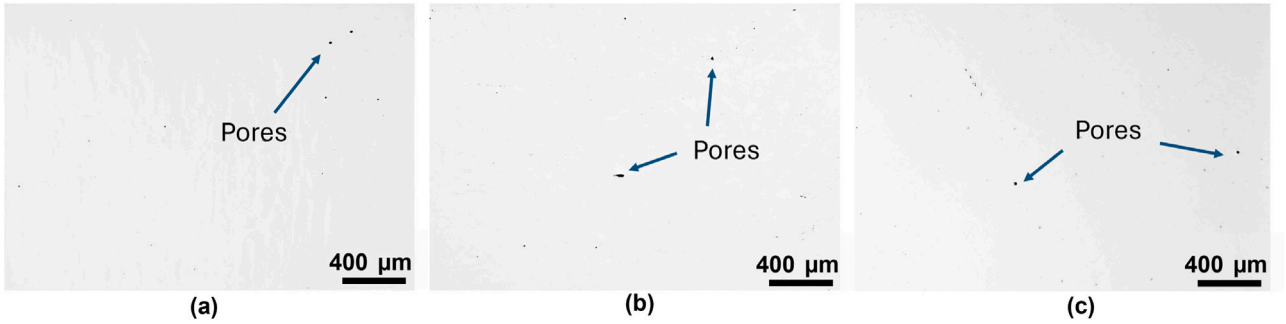

Fig. 4. Representative polished sections used for porosity assessment for (a) E_1 = 82.3 J/mm^3, (b) E_2 = 123.45 J/mm^3, and (c) E_3 = 222.22 J/mm^3. All three conditions exhibit high densification, with only sparse rounded pores and no visible lack-of-fusion defects.

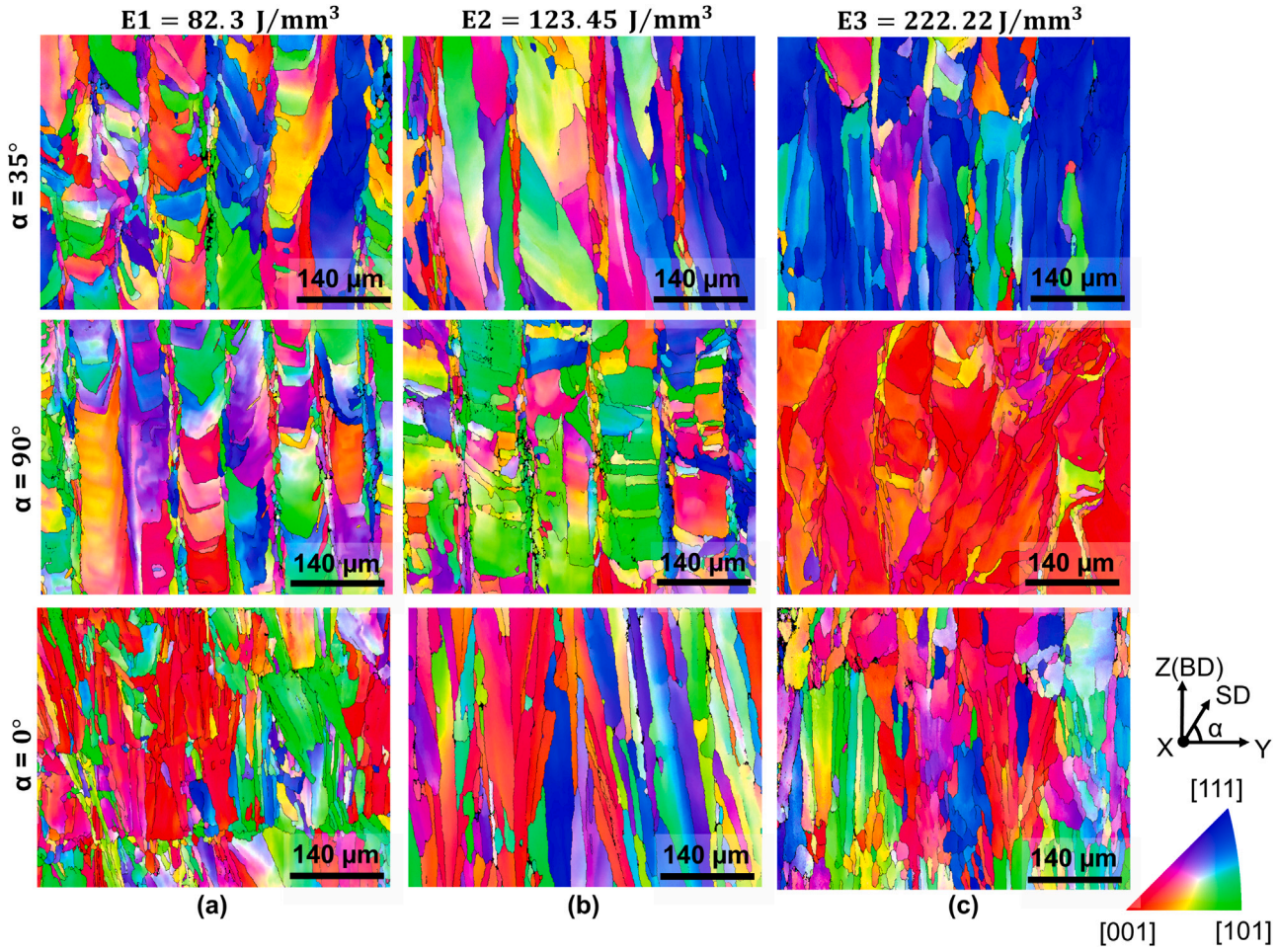

Fig. 5. IPF-X maps of the YZ sections for samples fabricated at three volumetric energy densities: 82.3 J/mm^3, 123.45 J/mm^3, and 222.22 J/mm^3. Rows correspond to scan angles α = 35°, 90°, and 0°, while columns correspond to the three energy densities. All maps are shown at the same magnification.

condition aligned with the scanning direction X(SD), as shown in Fig. 3. The specimen geometry had an overall length of 77 mm, a gauge length of 20 mm, a grip width of 6.7 mm, a thickness of 2.5 mm, and a transition radius of 20 mm. Tensile tests were performed using an Instron 5581 universal testing machine equipped with 50 kN grips. Strain was measured using a 10 mm extensometer (travel ±50%). The crosshead displacement rate was set to 1 mm/min. Engineering stress–strain curves were used to determine Young's modulus, the 0.2% proof stress $\sigma_{0.2}$ (0.2% offset method), the ultimate tensile strength (UTS), and the total elongation to fracture. Young's modulus was obtained by linear regression over the initial linear elastic segment of the extensometer-based stress–strain response, excluding the initial seating region.

2.2. Sample preparation and microstructure characterization tools

After fabrication, the samples were detached from the baseplate and sectioned along the YZ plane. Mechanical preparation proceeded through SiC papers from P80 to P1200, followed by diamond suspensions of 3 µm and 1 µm. Final surface finishing employed an oxide polishing suspension (OPS) to minimize surface deformation and improve electron backscatter diffraction (EBSD) pattern quality.

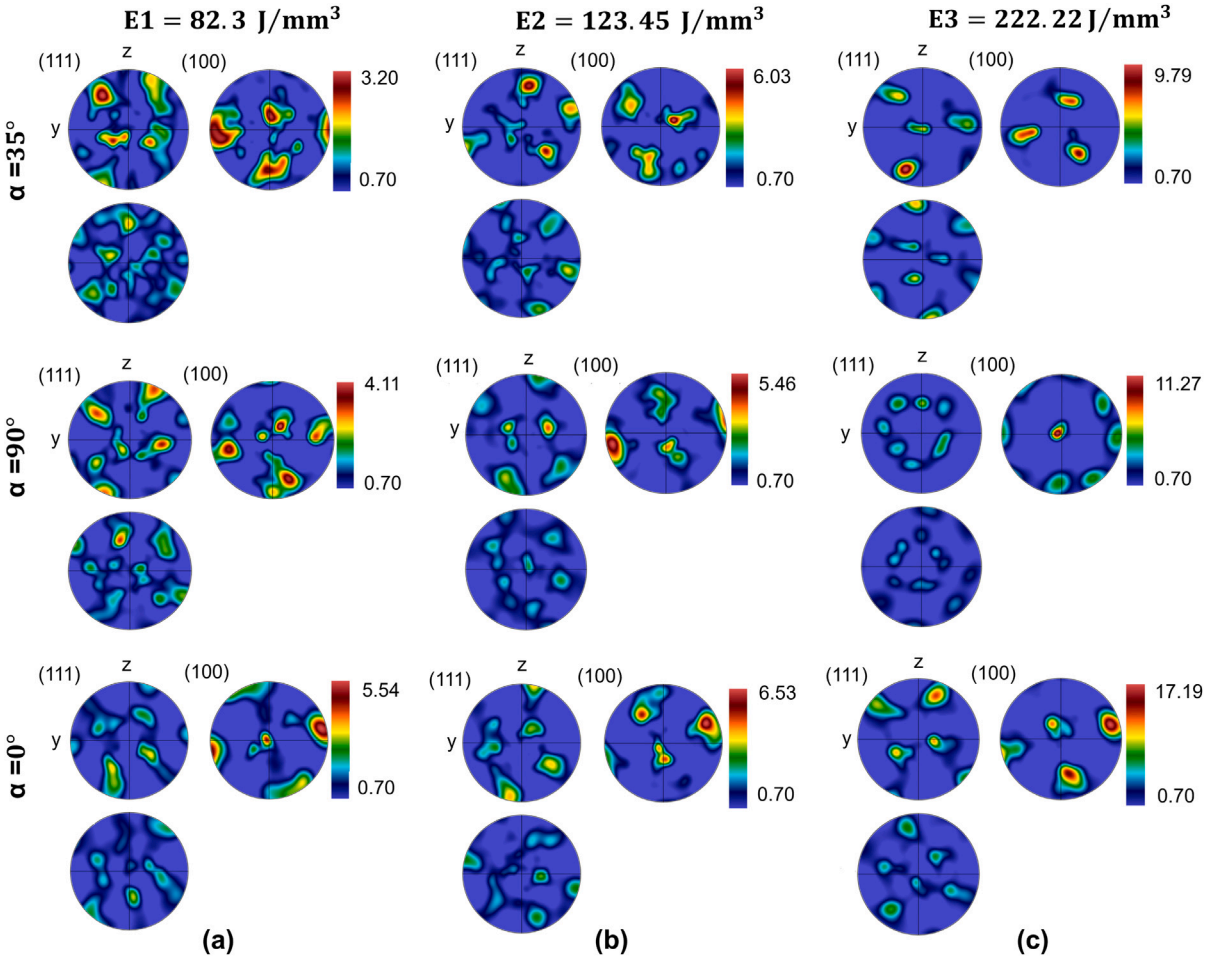

Fig. 6. Pole figures of the {111}, {100}, and {110} families for IN625 specimens fabricated at three volumetric energy densities: 82.3 J/mm^3, 123.45 J/mm^3, and 222.22 J/mm^3. Rows correspond to scan angles $\alpha = 35°$, 90°, and 0°, and columns correspond to the three energy-density conditions. The pole figures show that scan angle controls the dominant crystallographic component aligned with the scanning direction, while increasing energy density generally sharpens the texture, as reflected by the increase in maximum pole intensity. Intensities are given in multiples of random distribution (m.r.d.).

EBSD was performed on a Zeiss EVO MA-10 scanning electron microscope (SEM) equipped with a tungsten emitter and operated under high vacuum ($P < 10^{-5}$ Pa). A Nordif UF-1000 EBSD detector was used with TSL OIM Analysis software. Typical acquisition settings were 20 kV accelerating voltage, 10 nA probe current, and a step size of 1 μm. Data acquisition and indexing were carried out using NORDIF software; texture post-processing and analysis were performed with the ATEX software [16]. Pole-figure (PF) intensities are reported in multiples of a random distribution (m.r.d.); that is, PF densities are normalized to a random polycrystal (1 m.r.d. corresponds to random).

The texture index is written in compact form as [17]:

$$J = \int_{SO(3)} f(g)^2 \, dg \tag{2}$$

where: (i) SO(3) denotes the rotation group in three dimensions (the space of all crystal-to-sample orientations g); (ii) $f(g)$ is the orientation distribution function (ODF), a dimensionless probability density on SO(3) giving the volume fraction of material whose orientations lie in an infinitesimal neighbourhood dg about g. The ODF is normalized so that $\int_{SO(3)} f(g)\,dg = 1$ and a random texture corresponds to $f(g) \equiv 1$, hence $J = 1$ for random and $J > 1$ as preferred orientation strengthens.

We report (i) the peak PF intensity (m.r.d.) and (ii) the texture index J obtained from EBSD-derived ODFs using cubic sample and crystal symmetry appropriate for IN625. When relevant, the Taylor factor was estimated from the EBSD data to connect orientation with the expected ease of slip under the applied loading axis.

To reveal melt-pool boundaries and cellular/columnar features, polished sections were chemically etched in a solution of 92 % HCl, 3 % H_2SO_4, and 2 % HNO_3 for 5 s to 7 s. Optical microscopy was performed on a Zeiss Imager M2m equipped with a 5 megapixel Zeiss ICC5 camera at ×100 and ×500 magnifications for qualitative microstructure assessment and porosity evaluation.

Instrumented micro-indentation followed the Oliver–Pharr protocol using a Vickers indenter [18]. The maximum load was 2 N, loading and unloading rates were 4000 mN/min, the peak load was held for 5 s. Signals were sampled at 10 Hz, with contact detection at 10 mN. Unloading curves were fit over the 40 % to 98 % load window. A Poisson's ratio of $\nu = 0.30$ was used for IN625 in the analysis, and the instrument software reported Young's modulus E. To examine orientation-dependent elastic response and minimize indentation size effects, indent arrays were positioned using prior EBSD maps to target specific grain orientations (α = 90°, 35° and 0°). A two-row matrix of seven indents per row was applied; to avoid interaction between plastic zones, the centre-to-centre spacing was 150 μm between adjacent indents while the indent diameter was 40 μm. This layout provided a set of indentation moduli E for each scan-angle region, and each indent was cross-validated against local EBSD maps to assess crystallographic orientation and boundary proximity before reporting modulus trends.

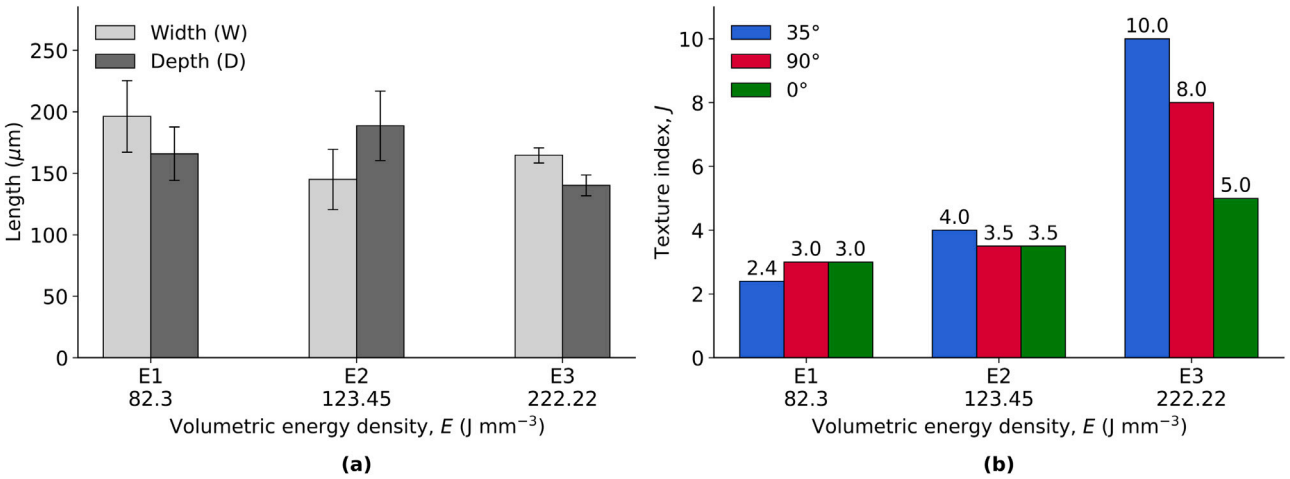

Fig. 7. Summary of (a) melt-pool width and height, and (b) texture index as a function of volumetric energy density for samples fabricated at scan angles $\alpha = 35°$, 90°, and 0°. Error bars represent ± one standard deviation.

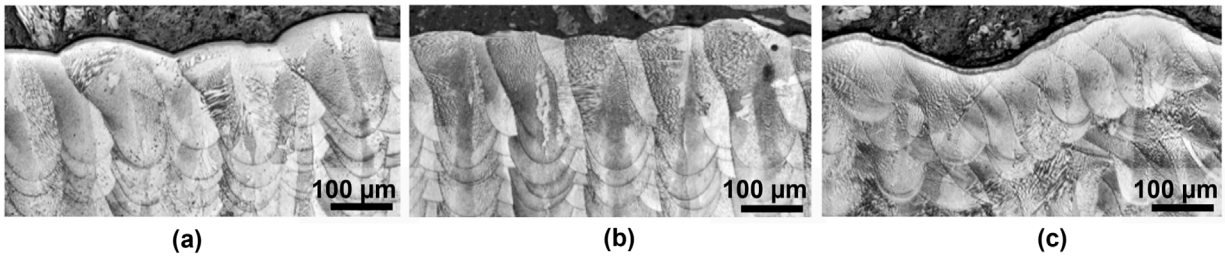

Fig. 8. Etched cross-sectional micrographs of the top layer showing melt-pool boundaries for three volumetric energy densities: (a) $E_1 = 82.3\,\mathrm{J/mm^3}$, (b) $E_2 = 123.45\,\mathrm{J/mm^3}$, and (c) $E_3 = 222.22\,\mathrm{J/mm^3}$.

3. Results and discussion

3.1. Laser scan angle and processing conditions control texture component selection and sharpening

Parallelepiped samples of 20 mm × 10 mm × 10 mm were successfully fabricated, and 10 mm × 10 mm × 10 mm cubes were extracted for each parameter set corresponding to the nominal energy labels $E1 = 82.3\,\mathrm{J/mm^3}$, $E2 = 123.45\,\mathrm{J/mm^3}$, and $E3 = 222.22\,\mathrm{J/mm^3}$. Representative polished sections show a high densification level for all three conditions, with sparse rounded pores and no evidence of lack-of-fusion defects (Fig. 4). Quantitative image analysis on ten optical micrographs per condition, summarized in Table 2, confirms that the measured porosity remained low for all parameter sets.

3.1.1. Crystallographic texture analysis

Inverse pole figure maps (Fig. 5), plotted parallel to the scanning direction (SD) from EBSD acquired on the YZ section, reveal two coupled effects of the processing conditions: scan angle controls the nature of the crystallographic component selected along SD, whereas the parameter set controls how strongly this component develops.

At E1, the $\alpha = 35°$ and $\alpha = 90°$ conditions both exhibit mixed grain orientations with significant local heterogeneity, including ⟨001⟩, ⟨101⟩, and ⟨111⟩ components parallel to SD. Several grains display colour gradients, indicating intragranular misorientation and competitive growth. For $\alpha = 0°$, the grains are elongated, but the distinction between fine grains nucleated near melt-pool bottoms and larger laterally inherited columnar grains is less clearly resolved than for $\alpha = 35°$ and $\alpha = 90°$.

At E2, decreasing the hatch spacing while keeping P/v constant preserves the same angle-dependent texture tendencies, but grain size increases and the microstructure becomes less directly constrained by the nominal hatch spacing. This effect is particularly visible for $\alpha = 90°$, where grains locally exceed the applied hatch distance.

At E3, while increasing P/v and reducing hatch spacing, the texture becomes markedly sharper. For $\alpha = 35°$, a dominant ⟨111⟩ ∥ SD component develops, whereas for $\alpha = 90°$, grains are predominantly oriented with ⟨001⟩ ∥ SD. The $\alpha = 0°$ condition remains more distributed, although the intensity of ⟨001⟩ related components increases relative to E1 and E2.

Pole figures (Fig. 6) and ODF derived texture indices confirm these observations. In Fig. 7, the texture index J increases from E1 to E3 for all scan angles, but the magnitude of this increase depends strongly on the scan path. The strongest sharpening is obtained for $\alpha = 35°$, where J reaches 10 at E3, followed by $\alpha = 90°$ with $J = 8$, whereas $\alpha = 0°$ remains comparatively weaker with $J = 5$. These trends are consistent with the pole figures. At E3, $\alpha = 35°$ exhibits the strongest ⟨111⟩ ∥ SD component, whereas $\alpha = 90°$ exhibits the strongest ⟨001⟩ ∥ SD component. By contrast, the $\alpha = 0°$ condition retains a broader distribution, even though its texture also sharpens at the highest-intensity condition.

Overall, the EBSD and ODF analyses show that scan angle primarily determines which crystallographic component aligns with the scanning direction, whereas the nominal processing condition mainly governs the sharpness of that selected component.

3.1.2. Melt-pool geometry and remelting continuity drive texture sharpening

Etched top-surface micrographs obtained for the $\alpha = 90°$ condition (Fig. 8) delineate the hatch tracks and melt-pool boundaries for each parameter set. Melt-pool depth D and width W were measured on six melt pools per condition using a calibrated pixel size. Since one side of each melt pool is partially remelted by the subsequent hatch, the total

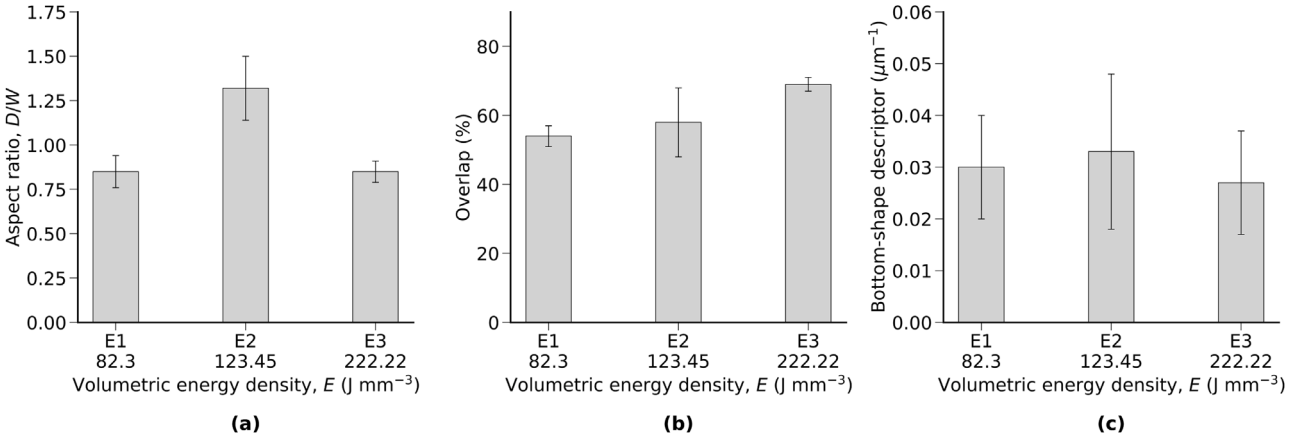

Fig. 9. Measured melt-pool geometric descriptors for the three nominal processing conditions: E_1 = 82.3 J/mm^3, E_2 = 123.45 J/mm^3, and E_3 = 222.22 J/mm^3 (mean ± SD, n = 6). (a) Melt-pool aspect ratio, D/W, showing the deeper and more vertically elongated pools obtained for E_2. (b) Track overlap ratio, which increases from E_1 to E_3. (c) Bottom-shape descriptor extracted from the digitized melt-pool bottom using the ImageJ Kappa plugin; in the present workflow, lower values correspond to a flatter average bottom profile. Together, these descriptors summarize the geometric differences used to interpret the texture-sharpening trends discussed in the text.

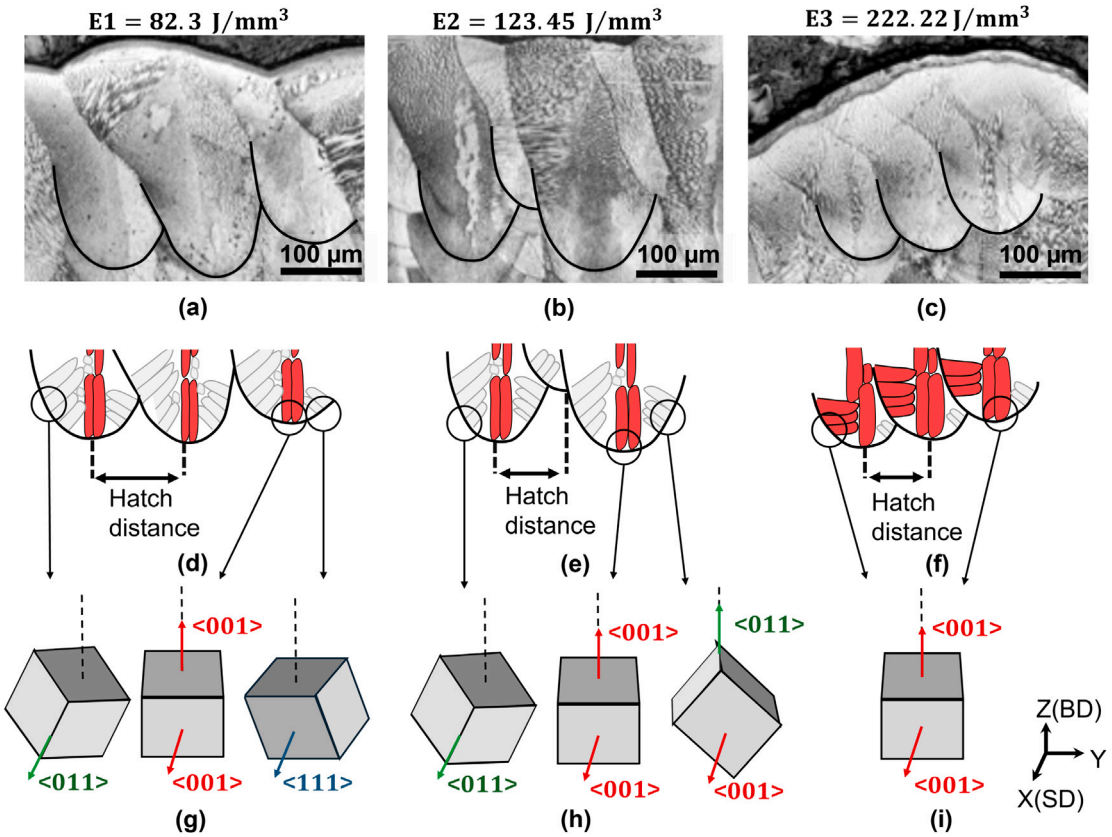

Fig. 10. Schematic interpretation of the correlation between melt-pool geometry, remelting continuity, crystallographic growth, and texture development. Columns (a), (b), and (c) correspond to parameter sets E1 (82.3 J/mm^3, P = 200 W, v = 900 mm/s, h = 0.09 mm), E2 (123.45 J/mm^3, P = 200 W, v = 900 mm/s, h = 0.06 mm), and E3 (222.22 J/mm^3, P = 150 W, v = 450 mm/s, h = 0.05 mm), respectively, all obtained for the α = 90° scan-angle condition. (a–c) Representative melt-pool cross-sections illustrating different melt-pool bottom profiles and associated non-remelted regions. (d–f) Corresponding mechanistic schematics showing melt-pool overlap, hatch distance, inferred local heat-flow directions, and the associated crystallographic growth paths within the remelted and non-remelted regions. (g–i) Idealized dominant grain orientations associated with the observed IPF colours, illustrating the transition from competing orientation inheritance in strongly curved melt pools (E1 and E2) to stronger orientation selection in flatter, more continuously remelted melt pools (E3). The specimen reference frame is shown at the lower right.

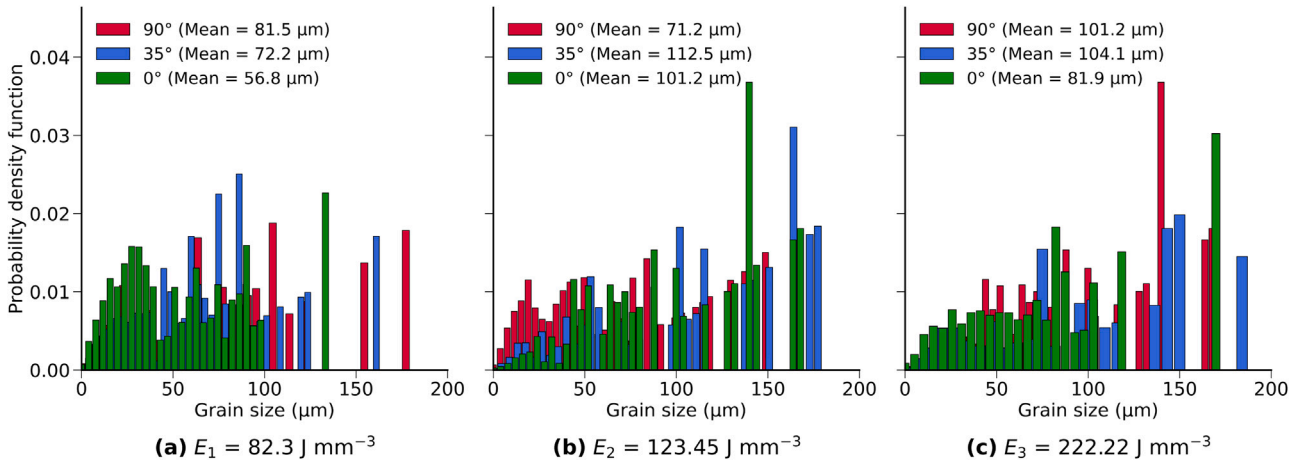

Fig. 11. Grain-size distributions for samples fabricated at different scan angles (90°, 35°, and 0°) under three nominal processing conditions: (a) $E_1 = 82.3\,J/mm^3$, (b) $E_2 = 123.45\,J/mm^3$, and (c) $E_3 = 222.22\,J/mm^3$. The corresponding mean grain sizes are indicated in each panel.

Table 4
IN625 single-crystal elastic constants and derived compliances at room temperature [19].

	C_{11} (GPa)	C_{12} (GPa)	C_{44} (GPa)	s_{11} (GPa^{-1})	s_{12} (GPa^{-1})	s_{44} (GPa^{-1})
Value	243.3	156.7	117.8	8.297×10^{-3}	-3.22×10^{-3}	8.489×10^{-3}

Table 5
Micro-indentation modulus and hardness by orientation class (mean ± standard deviation, $n = 6$). θ is the mean deviation angle between the crystal direction parallel to SD and the nearest ideal $\langle hkl \rangle$ family.

Orientation	θ (deg)	E_s (GPa)	E_r (GPa)	H_{IT} (GPa)
⟨100⟩	10.77 ± 1.82	159 ± 7	144 ± 6	3.43 ± 0.13
⟨110⟩	15.73 ± 2.42	243 ± 50	221 ± 19	3.66 ± 0.29
⟨111⟩	6.79 ± 1.15	297 ± 83	270 ± 75	3.34 ± 0.20

width was estimated as twice the visible half-width in order to maintain a consistent definition across all conditions.

The measured geometries (Fig. 7) show deep-penetration for all three parameter sets, with depths ranging from approximately 140 µm to 188 µm. However, the dimensional evolution is non-monotonic. From E1 to E2, reducing the hatch spacing increases the penetration depth from about 165 µm to 188 µm, while the apparent width decreases from about 196 µm to 144 µm. From E2 to E3, the simultaneous change in laser power, scan speed, and hatch spacing produces a shallower melt pool together with a slight widening relative to E2. These results show that the local melt-pool response cannot be described by a nominal scalar quantity alone, but depends on the coupled effects of scan speed, overlap, remelting history, and effective local energy absorption.

To relate melt-pool geometry to texture development, three experimentally measured descriptors were considered: the aspect ratio D/W, the overlap ratio, and a bottom-shape descriptor extracted from the ImageJ Kappa plugin along the digitized melt-pool boundary (Fig. 9). The bottom-shape descriptor quantifies the mean signed curvature of the fitted melt-pool bottom profile; in the present workflow, lower curvature values correspond to a flatter average bottom geometry. The values indicate that E2 exhibits the deepest and most vertically elongated melt pools ($D/W = 1.32$), whereas E1 and E3 display lower D/W values (~ 0.85). By contrast, the overlap ratio increases monotonically from 54% to 58% to 69% from E1 to E3, indicating progressively stronger remelting continuity between neighbouring tracks. The bottom-shape descriptor further indicates a flatter average melt-pool bottom for E3 than for E1 and E2. The geometric meaning of these descriptors is summarized schematically in Fig. 10.

These measured trends provide a consistent interpretation of the texture evolution. In E1 and E2, the larger effective non-remelted region beneath each track together with the more curved average melt-pool bottom are associated with a wider spread of local interface-normal directions. This favours competing epitaxial growth paths and therefore weaker texture sharpening. E2 is particularly instructive, although it exhibits the highest D/W ratio, it does not produce the sharpest texture. This shows that a high aspect ratio alone is not sufficient if remelting continuity remains limited and the local melt-pool shape is unstable from track to track. By contrast, E3 combines a smaller effective non-remelted region, the highest overlap ratio, and a flatter average bottom profile. A flatter melt-pool bottom implies a more uniform local growth direction across the pool base, which reduces orientation competition and favours more persistent epitaxial inheritance across successive tracks. In this sense, Fig. 10 should be understood as a mechanistic interpretation of how the measured melt-pool geometry promotes texture sharpening.

A further important observation is the forward/backward asymmetry of the melt-pool shape between adjacent tracks (Fig. 10e), which is visible for all parameter sets and is particularly pronounced for E2. Although the samples were oriented at 45° relative to the shielding-gas flow in order to reduce direct scan–gas-flow coupling, as suggested by Andreau et al. [12], this configuration can only mitigate rather than suppress such effects. A finite component of the scan direction remains aligned with the gas flow, so plume and process by-products may still be preferentially convected downstream, leading to unequal local interaction conditions on the two sides of adjacent tracks. The observed asymmetry is therefore interpreted primarily as evidence of residual scan-direction/gas-flow coupling affecting the local melt-pool shape. The stronger asymmetry observed for E2 suggests that this condition is more sensitive to such local perturbations, which may reduce remelting stability and thereby hinder persistent epitaxial inheritance and texture sharpening despite the large penetration depth. In the absence of in situ thermal diagnostics or validated thermal-fluid simulations, however, the present observations do not allow a unique attribution to a single transport mechanism. Such modelling would nevertheless be valuable in future work to quantify the local temperature field, remelting continuity, and track-to-track asymmetry under the different processing conditions, but it remains beyond the scope of the present experimental study.

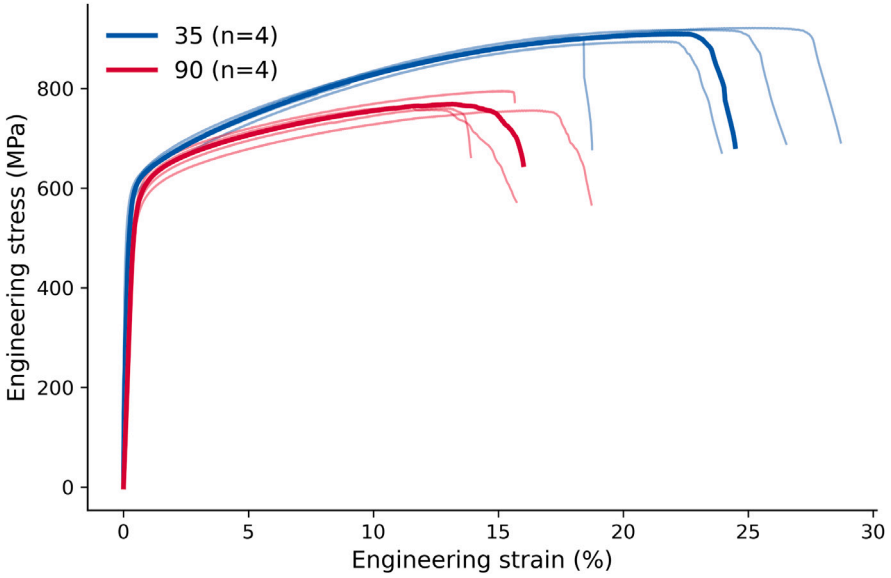

Fig. 12. Engineering stress–strain curves measured along the scanning direction for the 35° and 90° conditions. Thin lines correspond to individual tests and thick lines to the average response. The 35° condition, associated with a ⟨111⟩ dominated texture along scanning direction SD, exhibits higher strength and elongation than the 90° condition, associated with a ⟨100⟩ dominated texture along SD.

Table 6
Average tensile properties measured along the scanning direction (SD) for specimens representative of the 35° and 90° texture states. Values are reported as mean ± standard deviation ($n = 4$).

Condition	n	E (GPa)	$\sigma_{0.2}$ (MPa)	UTS (MPa)	Elongation (%)
35°	4	228.4 ± 17.4	596.3 ± 13.8	909.8 ± 12.7	24.5 ± 4.3
90°	4	132.9 ± 5.9	573.4 ± 16.3	768.7 ± 17.9	16.0 ± 2.0

Within this framework, the results can be rationalized by distinguishing texture selection from texture sharpening. Scan angle determines which crystallographic component becomes aligned with the scanning direction, whereas melt-pool geometry and track-to-track remelting conditions influence how strongly that selected component develops. Accordingly, the strongest SD-aligned textures are obtained for E3, with a dominant ⟨001⟩ ∥SD component for $\alpha = 90°$ and a dominant ⟨111⟩ ∥SD component for $\alpha = 35°$. These strongest textures are therefore associated not simply with higher nominal energy input, but with the parameter set showing the highest overlap ratio, a flatter average melt-pool bottom, and a smaller effective non-remelted region. The grain-size histograms in Fig. 11 support the same trend. E3 combines sharper texture with coarser grains, consistent with stronger epitaxial inheritance across neighbouring tracks. Under the present conditions, texture sharpening and grain coarsening can therefore develop simultaneously.

3.1.3. Scan-angle-induced textures produce distinct elastic and plastic responses along the scanning direction

To assess the mechanical consequences of the texture states selected by scan angle, local-scale elastic and plastic indicators were complemented by macroscopic tensile tests performed along the scanning direction (SD). In the present work, the theoretical orientation-dependent Young's modulus $E(\mathbf{n})$, indentation-derived modulus, and Taylor factor (TF) were used to rationalize the local response, while tensile testing was used to validate at the macroscopic scale the contrast between the two most distinct SD-aligned texture states.

Theoretical orientation-dependent modulus. For a cubic crystal, the uniaxial Young's modulus in direction $\mathbf{n} = (l_1, l_2, l_3)$ is given by [20]:

$$\frac{1}{E(\mathbf{n})} = s_{11} - 2\left(s_{11} - s_{12} - \tfrac{1}{2}s_{44}\right)\left(l_1^2 l_2^2 + l_2^2 l_3^2 + l_3^2 l_1^2\right), \tag{3}$$

where the compliance tensor components (s_{11}, s_{12}, s_{44}) are obtained from the elastic stiffness constants (C_{11}, C_{12}, C_{44}) through:

$$\begin{aligned} s_{11} &= \frac{C_{11} + C_{12}}{(C_{11} - C_{12})(C_{11} + 2C_{12})}, \\ s_{12} &= -\frac{C_{12}}{(C_{11} - C_{12})(C_{11} + 2C_{12})}, \\ s_{44} &= \frac{1}{C_{44}}. \end{aligned} \tag{4}$$

Using the room-temperature IN625 single-crystal elastic constants given in Table 4, the corresponding uniaxial moduli along the main high-symmetry directions are:

$$\langle 100\rangle : \mathbf{n} = (1,0,0) \quad \Rightarrow \quad E_{\langle 100\rangle} = 121\,\text{GPa},$$
$$\langle 110\rangle : \mathbf{n} = \left(\tfrac{1}{\sqrt{2}}, \tfrac{1}{\sqrt{2}}, 0\right) \quad \Rightarrow \quad E_{\langle 110\rangle} = 215\,\text{GPa},$$
$$\langle 111\rangle : \mathbf{n} = \left(\tfrac{1}{\sqrt{3}}, \tfrac{1}{\sqrt{3}}, \tfrac{1}{\sqrt{3}}\right) \quad \Rightarrow \quad E_{\langle 111\rangle} = 292\,\text{GPa}.$$

This theoretical ranking predicts a higher elastic modulus for ⟨111⟩ than for ⟨100⟩, and therefore provides the expected elastic trend for the SD-aligned texture states identified by EBSD.

Indentation modulus and local elastic response. Instrumented microindentation was used to probe the local elastic response associated with the different crystallographic orientations identified by EBSD. The experimental results (Table 5) show a clear orientation dependence consistent with the theoretical ranking $E_{\langle 111\rangle} > E_{\langle 110\rangle} > E_{\langle 100\rangle}$. In particular, the ⟨111⟩ class exhibits the highest average sample modulus, whereas the ⟨100⟩ class gives the lowest values [21].

The absolute values extracted by indentation are systematically higher than the ideal uniaxial $E(\mathbf{n})$ values. This difference is expected because the Oliver–Pharr analysis depends on the contact area estimate and because the measured response corresponds to a constrained multiaxial contact field rather than to a purely uniaxial loading direction.

In addition, given the indent size (40 μm) and the expected extent of the affected volume, some measurements may sample neighbouring orientations and grain boundaries, particularly in regions where ⟨110⟩ domains are smaller or adjacent to ⟨111⟩ areas. For this reason, the indentation-derived modulus is interpreted here as a local orientation sensitive indicator for a given orientation class, rather than as the intrinsic modulus of an isolated single grain. This also explains the larger scatter θ reported in Table 5 and observed for the ⟨110⟩ class,

for which both angular deviation from the ideal direction and local microstructural heterogeneity are more pronounced.

The indentation hardness H_{IT} varies only weakly between the three classes within the present scatter, indicating that hardness is less sensitive to elastic anisotropy than the modulus and is more strongly influenced by local heterogeneity and multislip deformation beneath the indent. Overall, the indentation results provide local-scale support that the SD-aligned textures identified in the EBSD analysis translate into measurable elastic contrast.

Taylor factor analysis for plastic response. To assess the plastic response associated with the different crystallographic orientations, Taylor factor averages were derived from the EBSD data using ATEX software [16], considering the 12 primary FCC {111}⟨110⟩ slip systems [22]. The results show the expected ranking: ⟨100⟩ exhibits the lowest Taylor factor (2.65 ± 0.15), ⟨110⟩ is intermediate (2.88 ± 0.12), and ⟨111⟩ exhibits the highest value (3.16 ± 0.10). This indicates that, for loading along SD, ⟨100⟩ oriented grains correspond to the softest state, whereas ⟨111⟩ oriented grains correspond to the hardest state.

Macroscopic tensile validation. To validate the texture-controlled mechanical response at the macroscopic scale, tensile tests were performed along the scanning direction (SD) on specimens fabricated separately under homogeneous 35° and 90° scan-angle conditions, using the same nominal processing parameters as in the microstructural study. These two conditions were selected because they exhibited the clearest contrast in SD-aligned texture state, namely a ⟨111⟩ dominated response for 35° and a ⟨100⟩ dominated response for 90°. Representative engineering stress–strain curves are shown in Fig. 12, and the mean tensile properties are summarized in Table 6.

In the plastic regime, the 35° condition reaches $\sigma_{0.2}$ = 596.3 ± 13.8 MPa and UTS = 909.8 ± 12.7 MPa, whereas the 90° condition gives $\sigma_{0.2}$ = 573.4 ± 16.3 MPa and UTS = 768.7 ± 17.9 MPa. The difference in yield strength remains moderate, consistent with the relatively small difference in average Taylor factor at slip onset. However, the larger separation at UTS indicates a higher work-hardening capacity for the ⟨111⟩ dominated state. This trend is consistent with the expected orientation dependence of plastic flow in FCC crystals, although the present study does not directly resolve slip activity or dislocation interactions [23].

Accordingly, the 35° condition also exhibits greater elongation to fracture (24.5 ± 4.3%) than the 90° condition (16.0 ± 2.0%). The coexistence of higher UTS and higher ductility in the ⟨111⟩ dominated state is therefore consistent with a higher work-hardening capacity, which delays plastic instability and extends the uniform deformation regime.

The tensile modulus follows the same overall trend as the theoretical and indentation-based elastic anisotropy. The mean tensile modulus is higher for the 35° condition (228.4 ± 17.4 GPa) than for the 90° condition (132.9 ± 5.9 GPa), providing macroscopic support for the stiffness contrast expected between ⟨111⟩ and ⟨100⟩ dominated states along the loading direction.

Taken together, the tensile results show that the scan-induced textures identified in the microstructural analysis produce distinct and measurable mechanical responses along SD. Under the present loading configuration, the ⟨111⟩ dominated state is associated with a stiffer response and with higher strength and ductility than the ⟨100⟩ dominated state. These macroscopic results therefore support the process–melt-pool–texture framework established above, rather than serving as a standalone demonstration of a known texture–property relation. The present findings are therefore directly relevant to as-built and lightly stress-relieved conditions and, more broadly, to the design of controlled initial microstructural states prior to any later thermal treatment, since post-build heat treatment may further modify the anisotropic microstructure and mechanical response of LPBF IN625 [24].

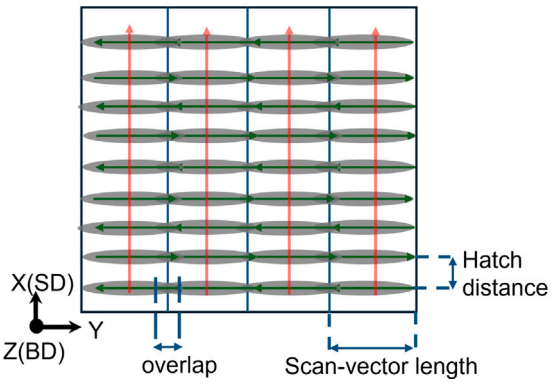

Fig. 13. Schematic interpretation of the short scan-vector-length (SVL) regime. Repeated short vectors progressively fill a confined scan band through adjacent partially overlapping melt pools. As the revisit time decreases, local reheating events accumulate within the band, so the thermal field is interpreted in terms of a laterally extended hot region rather than an isolated long-track melt pool. The schematic highlights the roles of scan-vector length in this short-SVL regime.

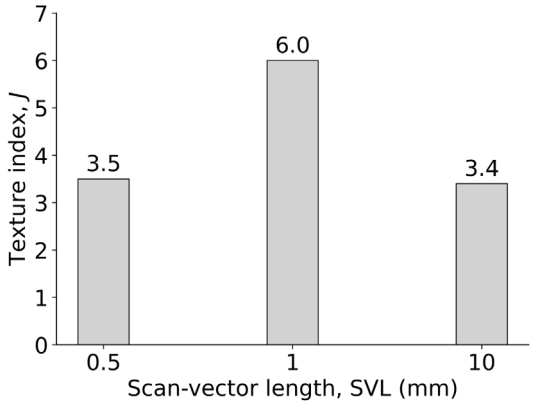

Fig. 14. Texture index J as a function of scan-vector length (SVL). Within the short-SVL comparison performed under identical nominal processing conditions, increasing SVL from 0.5 mm to 1.0 mm increases the texture index from 3.4 to 6.0, indicating stronger texture sharpening. The two short-SVL conditions were fabricated at E = 61.72 J/mm^3, whereas the long-vector reference was fabricated at E = 123.45 J/mm^3.

3.2. Short laser scan-vector length modifies local solidification and texture development through heat accumulation

To examine the role of scan-vector length (SVL) on solidification conditions and texture development, samples of 5 mm × 10 mm × 10 mm were produced using a constant 0° bidirectional scan strategy without inter-layer rotation (Fig. 1b).

In this set, the main objective was to assess whether scan-vector length can act as a mechanistic scan-path variable capable of modifying the development of a preferred crystallographic orientation, in particular a ⟨001⟩ type component along the scanning direction (SD). Two short values, 0.5 mm and 1.0 mm, were therefore selected to probe a regime dominated by repeated vector-end transients and local heat accumulation.

Under these conditions, the laser repeatedly accelerates and decelerates over a track length sufficiently short to increase the frequency of local revisit events, so the scan band cannot fully return to its initial thermal state between successive passes. This behaviour suggests the development of a laterally extended hot region that evolves as the band is progressively filled (Fig. 13). A useful characteristic timescale in this

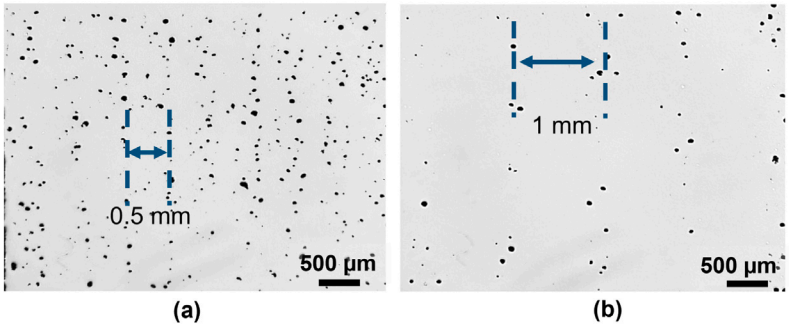

Fig. 15. Unetched surface micrographs of the short scan-vector length (SVL) conditions, showing defect clustering in the overlap and vector-end regions for (a) SVL = 0.5 mm and (b) SVL = 1 mm. Dashed lines indicate the periodic overlap bands associated with adjacent scan vectors.

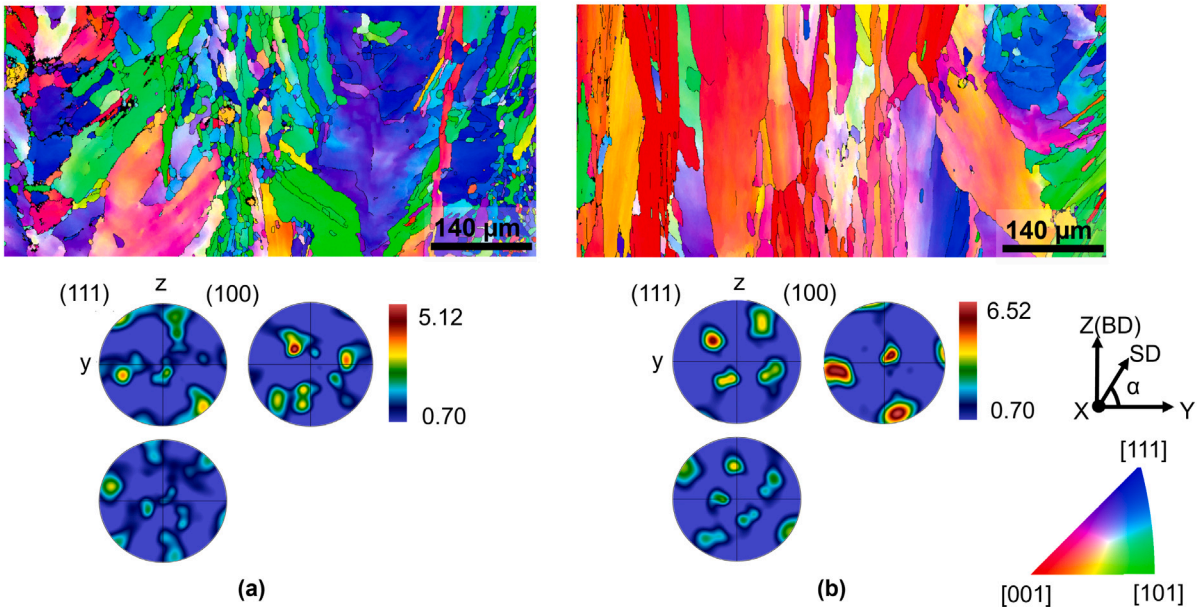

Fig. 16. IPF-X maps and corresponding {111}, {100}, and {110} pole figures for the short scan-vector-length (SVL) conditions: (a) SVL = 0.5 mm and (b) SVL = 1 mm. The comparison shows that increasing SVL from 0.5 to 1 mm promotes a clearer and sharper preferred orientation along the scanning direction, consistent with more stable remelting continuity and reduced texture competition. The inverse pole figure colour key and specimen reference frame are shown at the right.

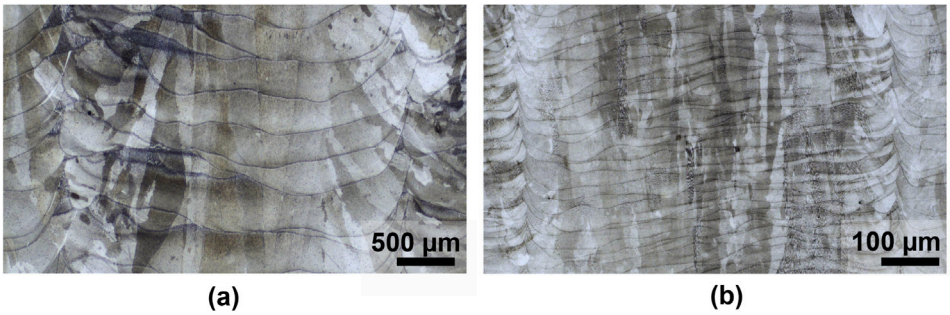

Fig. 17. Etched surface micrographs for the short scan-vector length (SVL) conditions, highlighting the scan band through adjacent partially overlapping melt pools for (a) SVL = 0.5 mm and (b) SVL = 1 mm. Panels (a) and (b) are shown at different magnifications to highlight the melt-pool features at each scale. More pronounced remelting features and vector-head/vector-tail disturbances are observed for SVL = 0.5 mm, consistent with stronger heat accumulation and more frequent solidification-front perturbations in this condition.

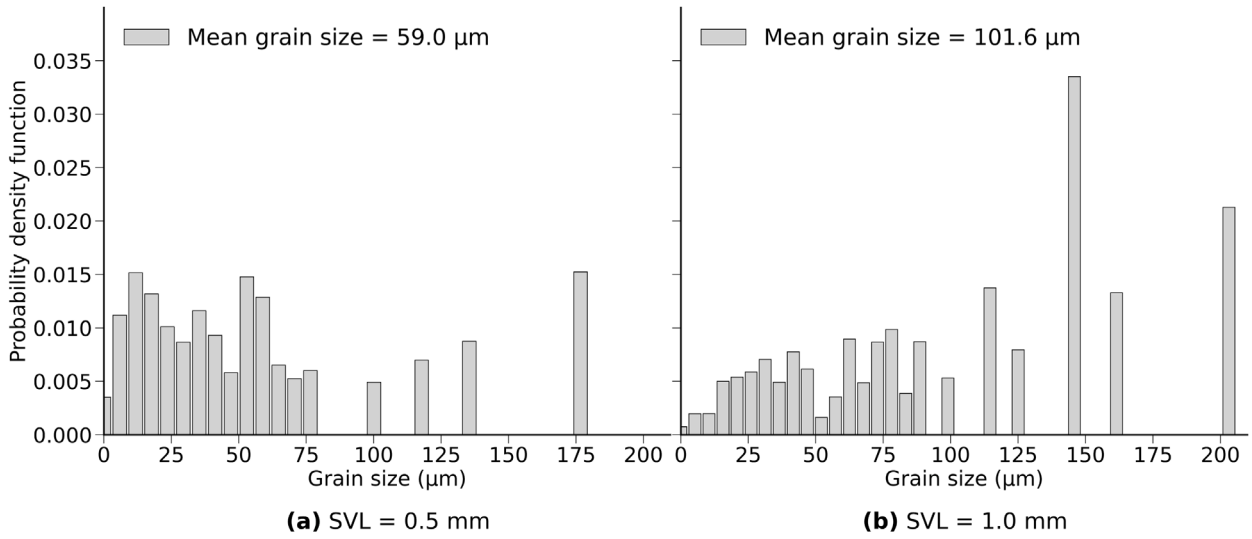

Fig. 18. Grain-size distributions for the short scan-vector length (SVL) conditions: (a) SVL = 0.5 mm and (b) SVL = 1 mm. The corresponding mean grain size is indicated in each panel.

context is the revisit time between successive local heating events

$$t_{\mathrm{rev}} \sim \frac{\mathrm{SVL}}{v}, \tag{5}$$

where SVL is the prescribed scan-vector length and v is the local scan speed along each vector. As SVL decreases, t_{rev} becomes shorter, so the material has less time to thermally relax before the neighbouring pass or the next vector-end event occurs.

The short-SVL conditions are therefore interpreted as being more susceptible to repeated local reheating, stronger heat accumulation within a confined band, and a higher frequency of vector-head/vector-tail perturbations. This interpretation is consistent with the observed defect clustering near vector ends and overlap regions, as well as with the distinct microstructural and textural responses obtained between SVL = 0.5 mm ($\mathrm{SVL}_{0.5}$) and SVL = 1 mm (SVL_{1}). For much longer vectors, such as SVL = 10 mm (SVL_{10}), these short-SVL specific effects are expected to be less pronounced, and the process is more appropriately viewed as a conventional localized long-track regime. The main comparison in this section is therefore between the two short-SVL conditions, 0.5 mm and 1.0 mm, which were produced under the same nominal processing conditions. The previously studied long-vector condition, denoted here as SVL_{10}, is retained only as a contextual reference for a conventional localized long-track regime under a 0° scan strategy. Because SVL_{10} was obtained under a different nominal processing condition, the comparison with SVL_{10} is used qualitatively only.

Representative cross-sections for $\mathrm{SVL}_{0.5}$ and SVL_{1} reveal a clear defect trade-off associated with the short-SVL regime. As shown in Fig. 15, porosity clusters concentrate preferentially in overlap and vector-end regions. The measured relative densities are 98.496 % for $\mathrm{SVL}_{0.5}$ and 98.705 % for SVL_{1}, compared with 99.9 % for the long-vector reference SVL_{10}. These short-SVL conditions should therefore be interpreted as deliberately amplified process states used to expose scan-path-induced thermal and textural effects, rather than as candidate production parameters.

EBSD analysis (Fig. 16) shows that the short-SVL conditions lead to clearly distinct microstructural and textural responses. For $\mathrm{SVL}_{0.5}$, the microstructure is dominated by equiaxed and short columnar grains, with mixed ⟨001⟩, ⟨101⟩, and ⟨111⟩ components in the overlap regions. The corresponding pole figures remain diffuse and the texture is weak, with a maximum intensity of 5.12 m.r.d. and a texture index of $J = 3.4$. The average grain size is 59 µm (Fig. 18), indicating limited persistence of directional growth.

By contrast, SVL_{1} produces clearly elongated columnar grains and a markedly sharper texture. A dominant ⟨001⟩ related cube component develops. In the IPF-X maps, this component is strengthened along the scanning direction, while the corresponding pole figures show that the associated ⟨100⟩ intensity maximum lies within approximately 10° of Z (BD), indicating a slightly tilted cube-related texture rather than an ideal exact alignment. The pole-figure intensity increases to 6.52 m.r.d. and the texture index reaches $J = 6$. At the same time, the average grain size increases to 101.6 µm. This increase in J from 3.4 for $\mathrm{SVL}_{0.5}$ to 6.0 for SVL_{1}, summarized in Fig. 14, shows that texture sharpening is maximized at the intermediate short-vector condition within the present SVL window. Compared with the 0.5 mm condition, the longer scan segment is inferred to allow a more persistent directional thermal field to develop within the band, which favours epitaxial growth and stronger competitive selection. Within the present short-SVL window, this condition is therefore the most effective for promoting the targeted ⟨001⟩ type component along SD.

The etched surfaces (Fig. 17) support this interpretation. For $\mathrm{SVL}_{0.5}$, the repeated vector ends and strong local heat accumulation are associated with a wider and more persistently hot molten region, together with frequent remelting disturbances at band boundaries and overlap zones. This condition is consistent with a less stable heat-flow direction, reduced effective directional solidification, and therefore weaker texture development. Similar vector-end overheating effects have been reported in PBF-LB/M by Li et al. [13]. The term 'burn-in' was first introduced by Goodarzi et al. [25] in the context of laser cladding to describe localized overheating at vector heads, and is adopted here by analogy. In the present work, this regime is interpreted as favouring repeated perturbation of the solidification front, which explains the weaker texture and more equiaxed grain morphology.

For SVL_{1}, heat accumulation still occurs, but the longer steady scanning segment allows a more directional and persistent thermal field to develop before the next vector-end perturbation. Compared with $\mathrm{SVL}_{0.5}$, the heat flow is therefore more coherent over the band width, which favours epitaxial growth and enhances competitive grain selection. This explains the sharper ⟨001⟩ texture and the coarser columnar microstructure observed in Figs. 16 and 18.

The long-vector reference SVL_{10} exhibits elongated grains with an average size of 101.2 µm and a lower texture index ($J = 3.5$) than SVL_{1}. Because SVL_{10} was produced under a different nominal processing condition, this comparison is not used as direct proof of an SVL-only effect. Instead, it is used qualitatively to contrast two distinct scanning regimes: a conventional localized long-vector melt-pool regime and

a short-SVL band-filling regime. The present qualitative comparison suggests that the SVL_1 condition can promote stronger texture sharpening than the long-vector reference, although this comparison cannot be interpreted as an SVL only effect because the nominal processing conditions differ.

Overall, the present results show that short scan-vector length can act as a mechanistic scan-path variable that modifies the local solidification regime in LPBF-processed IN625. Within the present parameter window, reducing SVL increases the influence of local heat accumulation and vector-end perturbations, which strongly affects grain morphology and texture development. The comparison between $SVL_{0.5}$ and SVL_1 indicates that excessively short vectors promote defect formation and weaken texture, whereas a moderate short SVL preserves stronger directional growth and produces a sharper ⟨001⟩ type texture along SD. In this sense, SVL affects texture not only as a geometric programming parameter, but through its influence on revisit time, local remelting continuity, and the persistence of the directional thermal field. At the same time, the associated defect clustering shows that the present short-SVL regime should be regarded as a mechanistic probe of process–texture coupling rather than as an optimized industrial processing route.

4. Conclusion

This work shows that crystallographic texture in PBF-LB/M processed IN625 can be systematically steered through scan-path design by controlling both dominant growth direction and the thermal conditions governing its persistence. The study establishes a coherent process–melt-pool–texture–property framework linking scan-path variables to solidification conditions, grain morphology, and macroscopic mechanical response.

First, the scan angle α primarily selects the dominant crystallographic component aligned with the scanning direction: ⟨111⟩ for $\alpha = 35°$ and ⟨001⟩ for $\alpha = 90°$. Variations in (P, v, h) then govern how strongly this selected component develops. The melt-pool analysis shows that the effective thermal history cannot be reduced to nominal volumetric energy density alone: overlap ratio, remelting continuity, melt-pool geometry, and local track-to-track variability all contribute independently to the final texture state. Across the tested parameter sets, conditions associated with a more uniform heat-flow direction and stronger remelting continuity produce sharper textures and more persistent epitaxial inheritance.

Second, short scan-vector length (SVL) introduces an additional mechanistic lever within a 0° strategy by modifying local heat accumulation and the frequency of vector-end perturbations. Very short vectors (SVL=0.5 mm) promote a strongly transient solidification regime associated with defect clustering, weaker texture, and a more equiaxed microstructure. A moderate short SVL (SVL=1.0 mm) preserves sufficient directional stability to strengthen competitive epitaxial growth, producing coarse columnar grains and a sharper ⟨001⟩ texture. Relative to the long-vector reference SVL_{10}, this result suggests that short-SVL band filling can promote stronger texture sharpening, although the comparison remains qualitative given the different nominal processing condition of the reference.

Finally, the scan-path-induced texture states translate into measurable and substantial mechanical differences along the scanning direction (SD). The theoretical elastic anisotropy ranking $E_{\langle 111\rangle} > E_{\langle 100\rangle}$ is confirmed by indentation measurements and further validated by tensile testing: the 35° condition (⟨111⟩ dominated texture along SD) exhibits a UTS of ≈ 910 MPa and elongation of 24.5 %, compared with ≈ 769 MPa and ≈ 16.0 % for the 90° condition (⟨001⟩ dominated texture along SD). The coexistence of higher strength and greater ductility in the ⟨111⟩ state reflects its higher work-hardening capacity, which sustains plastic flow to larger strains before the onset of instability.

The main scientific outcome is that scan-path design affects texture through two distinct but coupled roles: scan angle governs texture selection, whereas remelting continuity and SVL-induced thermal transients govern texture sharpening. This distinction provides a transferable framework for understanding and exploiting scan-path design as a texture-control strategy in PBF-LB/M alloys beyond the specific IN625 case studied here. Future work will build on these results to design and mechanically characterize architectured components combining spatially controlled texture states, supported by micromechanical modelling to establish quantitative structure–property relationships for scan-path-engineered PBF-LB/M components.

CRediT authorship contribution statement

Oumayma Elmaalouf: Writing – original draft, Software, Methodology, Investigation. **Patrice Peyre:** Writing – review & editing, Supervision, Methodology, Investigation, Conceptualization. **Stefan Dietrich:** Writing – review & editing, Supervision, Methodology, Conceptualization. **Corinne Dupuy:** Writing – review & editing, Investigation. **Justin Dirrenberger:** Writing – review & editing, Supervision, Methodology, Conceptualization.

Declaration of competing interest

The authors declare that they have no known competing financial interests or personal relationships that could have appeared to influence the work reported in this paper.

References

[1] ISO/ASTM, Additive manufacturing – general principles – fundamentals and vocabulary, 2021, Standard.
[2] W.E. Frazier, Metal additive manufacturing: a review, J. Mater. Eng. Perform. 23 (6) (2014) 1917–1928, http://dx.doi.org/10.1007/s11665-014-0958-z.
[3] T. DebRoy, H. Wei, J. Zuback, T. Mukherjee, J. Elmer, J. Milewski, A. Beese, A. Wilson-Heid, A. De, W. Zhang, Additive manufacturing of metallic components—Process, structure and properties, Prog. Mater. Sci. 92 (2018) 112–224, http://dx.doi.org/10.1016/j.pmatsci.2017.10.001.
[4] S. Khairallah, A. Anderson, A. Rubenchik, W. King, Laser powder-bed fusion additive manufacturing: physics of complex melt flow and formation mechanism of pores, spatter, and denudation zones, Acta Mater. 108 (2016) 36–45, http://dx.doi.org/10.1016/j.actamat.2016.02.014.
[5] C. Zhao, B. Shi, S. Chen, D. Du, T. Sun, B.J. Simonds, K. Fezzaa, A.D. Rollett, Laser melting modes in metal powder bed fusion additive manufacturing, Rev. Modern Phys. 94 (4) (2022) 045002, http://dx.doi.org/10.1103/RevModPhys.94.045002.
[6] X. Luo, T. Song, A. Gebert, K. Neufeld, I. Kaban, H. Ma, W. Cai, H. Lu, D. Li, N. Li, Y. Li, C. Yang, Programming crystallographic orientation in additive-manufactured beta-type titanium alloy, Adv. Sci. 10 (23) (2023) 2302884, http://dx.doi.org/10.1002/advs.202302884.
[7] K. Sofinowski, S. Raman, X. Wang, B. Gaskey, M. Seita, Layer-wise engineering of grain orientation (LEGO) in laser powder bed fusion of stainless steel 316L, Addit. Manuf. 38 (2021) 101809, http://dx.doi.org/10.1016/j.addma.2020.101809.
[8] S.-H. Sun, K. Hagihara, T. Nakano, Effect of scanning strategy on texture formation in Ni-25 at.% Mo alloys fabricated by selective laser melting, Mater. Des. 140 (2018) 307–316, http://dx.doi.org/10.1016/j.matdes.2017.11.060.
[9] J. Marattukalam, D. Karlsson, V. Pacheco, P. Beran, U. Wiklund, U. Jansson, B. Hjörvarsson, M. Sahlberg, The effect of laser scanning strategies on texture, mechanical properties, and site-specific grain orientation in selective laser melted 316L SS, Mater. Des. 193 (2020) 108852, http://dx.doi.org/10.1016/j.matdes.2020.108852.
[10] M.L. Montero-Sistiaga, R. Mertens, B. Vrancken, X. Wang, B. Van Hooreweder, J.-P. Kruth, J. Van Humbeeck, Changing the alloy composition of Al7075 for better processability by selective laser melting, J. Mater. Process. Technol. 238 (2016) 437–445, http://dx.doi.org/10.1016/j.jmatprotec.2016.08.003.
[11] V. Popovich, E. Borisov, A. Popovich, V. Sufiiarov, D. Masaylo, L. Alzina, Functionally graded inconel 718 processed by additive manufacturing: Crystallographic texture, anisotropy of microstructure and mechanical properties, Mater. Des. 114 (2017) 441–449, http://dx.doi.org/10.1016/j.matdes.2016.10.075.
[12] O. Andreau, I. Koutiri, P. Peyre, J. Penot, N. Saintier, E. Pessard, T. Terris, C. Dupuy, T. Baudin, Texture control of 316L parts by modulation of the melt pool morphology in selective laser melting, J. Mater. Process. Technol. 264 (2019) 21–31, http://dx.doi.org/10.1016/j.jmatprotec.2018.08.049.
[13] L. Li, H. Chen, X. Wang, Z. Liao, Effects of vector length on the melt-pool morphology and grain structure characteristics of alloy 718 in laser powder bed fusion, J. Mater. Process. Technol. 326 (2024) 118317, http://dx.doi.org/10.1016/j.jmatprotec.2024.118317.

[14] S. Shahabad, A. Usman, Z. Zhang, A. Keshavarzkermani, R. Esmaeilizadeh, A. Bonakdar, E. Toyserkani, On the effect of thin-wall thickness on melt pool dimensions in laser powder-bed fusion of hastelloy X: Numerical modeling and experimental validation, J. Manuf. Process. 75 (2022) 435–449, http://dx.doi.org/10.1016/j.jmapro.2022.01.029.

[15] T. Ishimoto, S. Wu, Y. Ito, S. Sun, H. Amano, T. Nakano, Crystallographic orientation control of 316L austenitic stainless steel via selective laser melting, ISIJ Int. 60 (8) (2020) 1758–1764, http://dx.doi.org/10.2355/isijinternational.ISIJINT-2019-744.

[16] B. Beausir, J.-J. Fundenberger, Analysis Tools for Electron and X-ray Diffraction (ATEX-software), Université de Lorraine, Metz, France, 2017, URL http://www.atex-software.eu.

[17] H.-J. Bunge, C. Esling, Quantitative Texture Analysis, Deutsche Gesellschaft für Metallkunde, Oberursel, Germany, 1982.

[18] W. Oliver, G. Pharr, Measurement of hardness and elastic modulus by instrumented indentation: Advances in understanding and refinements to methodology, J. Mater. Res. 19 (1) (2004) 3–20, http://dx.doi.org/10.1557/jmr.2004.19.1.3.

[19] S. Saha, O. Kafka, Y. Lu, C. Yu, W. Liu, Macroscale property prediction for additively manufactured IN625 from microstructure through advanced homogenization, Integr. Mater. Manuf. Innov. 10 (2021) 360–372, http://dx.doi.org/10.1007/s40192-021-00221-8.

[20] G. Dieter, Mechanical Metallurgy, third ed., McGraw-Hill, New York, 1986.

[21] J. Pérez-Ruiz, F. Galbusera, L. Caprio, P. Barbara, L. LÓpez de lacalle, A. Lamikiz, A. Demir, Laser beam shaping facilitates tailoring the mechanical properties of IN718 during powder bed fusion, J. Mater. Process. Technol. 328 (2024) 118393, http://dx.doi.org/10.1016/j.jmatprotec.2024.118393.

[22] J. Chen, Z. Liu, C. Liu, B. Zhang, T. Liu, G. Chen, M. Qin, X. Qu, Effects of scanning strategy and scanning speed on microstructures and mechanical properties of NiTi alloys by laser powder bed fusion, Mater. Sci. Eng.: A 914 (2024) 147115, http://dx.doi.org/10.1016/j.msea.2024.147115.

[23] G.I. Taylor, Plastic Strain in Metals, Journal of the Institute of Metals, Institute of metals, 1938.

[24] J. Zhu, K. Feng, H. Kokawa, Z. Li, Effect of heat treatment on the anisotropic mechanical properties and corrosion resistance of laser powder bed fusion fabricated Inconel 625, J. Alloys Compd. 1001 (2024) 175087, http://dx.doi.org/10.1016/j.jallcom.2024.175087.

[25] D. Goodarzi, J. Pekkarinen, A. Salminen, Effect of process parameters in laser cladding on substrate melted areas and the substrate melted shape, J. Laser Appl. 27 (S2) (2015) S29201, http://dx.doi.org/10.2351/1.4906376.